Numerical Simulation of Transient Combustion Process in Pulse Detonation Engine

Hyungwon Kim* Dale A. Anderson† Frank K. Lu‡ and Donald R. Wilson§
University of Texas at Arlington, Arlington, Texas 76019

A two-dimensional time-accurate numerical model to simulate the transient combustion process in a pulse detonation engine is presented. For the purpose of constructing an efficient numerical tool, while maintaining a reasonable accuracy, a two-step global model has been selected and validated for a hydrogen–air mixture. The inherent stiffness in the chemical reaction model is properly taken care of by the point-implicit treatment of source terms, together with the application of a Local Ignition Averaging Model to each mesh where ignition starts. A series of calculations is performed using different orders of numerical schemes in spatial and temporal accuracy and different mesh sizes to select a proper scheme and a mesh size to provide adequate resolution of the physical process. The calculated results from the present model are compared with the theoretical Chapman–Jouguet data. A simulation of a shock-induced detonation experiment is also performed to provide a validation of the present model in the unsteady propagation of a detonation wave and its interactions with the boundaries as well as other waves.

Introduction

The pulse detonation engine (PDE) has received considerable interest in recent years due to its potential advantages in performance and inherent simplicity over current propulsion concepts. The PDE uses detonation waves that are initiated repeatedly at either end of a detonation chamber and propagate through a fuel–oxidizer mixture with supersonic speed to produce high pressure which is the main thrusting mechanism. This rapid detonation process permits the PDE to achieve nearly constant volume combustion resulting in better efficiencies compared with the usual constant pressure Brayton cycle. In addition, the PDE does not necessarily need a compressor or a turbine, and this makes the engine mechanically simple and cost effective. Furthermore, PDE's can be operated in a wide range of flight speeds, from low subsonic to high supersonic, regardless of the engine size and shape [1]–[4].

Conceptually there seems to be no doubt that the PDE will be a good alternative to conventional engines, as well as a revolutionary propulsion system for future space transportation. However, there are still many problems to be solved and many complex phenomena to be understood for the PDE to be operable in a real world. Detonation initiation, the PDE cycle analysis and optimization are included among the problems [5, 6].

*Research Associate, Mechanical and Aerospace Engineering Department. Student member AIAA.

†Professor, Mechanical and Aerospace Engineering Department. Associate Fellow AIAA.

‡Professor and Director, Aerodynamics Research Center, Mechanical and Aerospace Engineering Department. Associate Fellow AIAA.

§Professor and Chairman, Mechanical and Aerospace Engineering Department. Associate Fellow AIAA.

The PDE can be classified as an unsteady propulsion engine which operates in an intermittent manner governed by a cycle frequency. The cycle frequency of the PDE is defined as the inverse of the time required to complete a full detonation cycle. One full cycle is comprised of several distinct processes: (a) filling the chamber with a fresh fuel/oxidizer mixture, (b) initiating detonation, (c) propagation of detonation waves, and (d) expansion of burned gases to reduce the chamber pressure to the refill level. All of these processes are interdependent, and the interaction and timing are crucial to multi-cycle engine efficiency. Time-accurate computational fluid dynamics (CFD) methods can be used to perform cycle analysis and performance optimization of the PDE from the simulations of the corresponding flow fields with variations in design parameters.

This paper presents an unsteady numerical simulation model for these purposes. The key words here are accuracy and efficiency. The objective of this work is to construct a two-dimensional time-accurate numerical simulation model to be used for PDE's, efficient enough for design parametric studies while maintaining a reasonable accuracy. The simulation model is constructed to formulate the corresponding physical phenomena as precisely as possible including chemical and thermal non-equilibrium, and to numerically solve the resulting mathematical formulation as accurately as possible. The novel aspect of this work includes a combination of point-implicit treatment and Local Ignition Averaging applied to the global two-step reaction model for efficient time-accurate solution of a propagating detonation wave. The partition of internal energy is based on the two-temperature model, and the vibrational energy of each species is obtained by subtracting out fully-excited translational and rotational energy from total internal energy. Roe's flux-difference split scheme is combined with the Runge–Kutta integration scheme for an accurate capture of the shock wave both in space and in time.

The present model is validated by comparing the calculated results with the theoretical CJ and experimental data. Shock-induced detonation experiments are simulated to provide a validation of the numerical model, and as an aid in understanding the experimental results. Extensive calculations are performed with numerical schemes of different orders in space and time, and with different mesh sizes to select the proper scheme and mesh size providing adequate resolution of the physical process.

Mathmatical Formulation

Governing Equations

The time-dependent conservation equations governing inviscid, non-heat-conducting, reacting gas flow in which thermal nonequilibrium is modeled with a two-temperature approximation are written in the conservation law form. This form is advantageous in numerical simulations to correctly capture shock waves [7]. In two dimensional Cartesian coordinate system, this takes the following form:

$$\frac{\partial U}{\partial t} + \frac{\partial F}{\partial x} + \frac{\partial G}{\partial y} = S \tag{1}$$

where U is the vector of conserved variables, F and G are the convective flux vectors, and S is the vector of source terms. Each vector is written as

$$U = \begin{bmatrix} \rho_s \\ \rho u \\ \rho v \\ \rho e_v \\ \rho E \end{bmatrix}, \quad F = \begin{bmatrix} \rho_s u \\ \rho u^2 + p \\ \rho uv \\ \rho u e_v \\ \rho u E + pu \end{bmatrix},$$

$$G = \begin{bmatrix} \rho_s v \\ \rho uv \\ \rho v^2 + p \\ \rho v e_v \\ \rho v E + pv \end{bmatrix}, \quad S = \begin{bmatrix} w_s \\ 0 \\ 0 \\ w_v \\ 0 \end{bmatrix} \tag{2}$$

In this equation, subscript s ranges 1 to N_s, where N_s is the number of species. The first N_s rows represent species continuities, followed by two momentum conservation equations for the mixture. The next row describes the rate of change in the vibrational energy, and the final row is the total energy conservation equation. In the above equation, u and v are the velocities in the x and y direction respectively, ρ is the mixture density, p is the pressure, e_v is the vibrational energy, and E is the total energy per unit mass of mixture. ρ_s is the s-th species density, w_s is the mass production rate of species s per unit volume, and w_v is the vibrational energy source term which is defined as

$$w_v = \sum_s Q_{vs} + \sum_s w_s e_{d,s} \tag{3}$$

Here, Q_{vs} represents the vibrational energy exchange rate of species s due to the relaxation process with translational energy, and the second term, $w_s e_{d,s}$ represents the amount of vibrational energy gained or lost due to production or depletion of species s from chemical reactions.

Thermodynamic Properties

A general representation of species internal energy includes a portion of the internal energy in thermodynamic equilibrium and the remaining portion in a nonequilibrium state. The equilibrium portion of the internal energy is the contribution due to translation and internal modes that can be assumed to be in equilibrium at the translational temperature T. The remaining nonequilibrium portion is the contribution due to internal modes that are not in equilibrium at the translational temperature T, but may be assumed to satisfy a Boltzman distribution at a different temperature.

For the temperature range of interest, the rotational mode is assumed to be fully excited and in equilibrium with translational temperature T, while the electronic excitation and free electron modes can be safely ignored. Thus, the only remaining energy mode that could be in nonequilibrium with translational temperature T is the vibrational energy mode. Therefore, the species internal energy based on the two-temperature model can be written as follows:

$$e_s = e_{eq,s}(T) + e_{v,s}(T_v) \tag{4}$$

where $e_{eq,s}$ is the equilibrium portion of the internal energy and $e_{v,s}$ is the vibrational energy which is not in thermodynamic equilibrium. The equilibrium portion of the energy can be further defined as

$$e_{eq,s} = \int_{T_{ref}}^{T} (C^s_{v,t} + C^s_{v,r})\, d\tau + e_{s,o} \tag{5}$$

where T_{ref} is the reference temperature, $e_{s,o}$ is the energy of formation, and $C^s_{v,t}$ and $C^s_{v,r}$ are the translational and rotational portion of specific heat at constant volume, respectively. Since the translational and rotational modes are assumed to be fully excited, $C^s_{v,t}$ and $C^s_{v,r}$ can be written as

$$C^s_{v,t} = 1.5\bar{R}/M_s \tag{6}$$

$$C^s_{v,r} = \begin{bmatrix} \bar{R}/M_s, & \text{diatomic molecule} \\ 1.5\bar{R}/M_s, & \text{polyatomic molecule} \end{bmatrix} \tag{7}$$

where R is the universal gas constant and M_s is the molecular weight of species s. The energy of formation $e_{s,o}$ can be obtained from readily available heat of formation data as

$$e_{s,o} = h_{s,o} - \frac{\bar{R}}{M_s} T_{ref} \tag{8}$$

Therefore, the equilibrium portion of energy can be written as follows:

$$e_{eq,s}(T) = K_s \frac{\bar{R}}{M_s}(T - T_{ref}) - \frac{\bar{R}}{M_s} T_{ref} + h_{s,o} \tag{9}$$

where K_s is 1.5, 2.5, 3.0 for monatomic, diatomic or linear polyatomic, and nonlinear polyatomic species respectively.

The heat capacity of the vibrational energy mode can now be obtained from the fact that the translational

and rotational heat capacities are independent of temperature. This can be evaluated by utilizing the readily available curve fit for total heat capacity evaluated at temperature T_v and subtracting out the constant contributions from the translation and rotational heat capacities as follows:

$$C^s_{v,v}(T_v) = C^s_v(T_v) - C^s_{v,t} - C^s_{v,r} \tag{10}$$

where

$$C^s_v(T_v) = C^s_p(T_v) - \frac{\bar{R}}{M_s}$$

C^s_v and C^s_p are specific heats at constant volume and constant pressure respectively, and curve fit data for $C^s_p(T)$ can be found in the following form [8, 9]:

$$C^s_p(T) = \frac{\bar{R}}{M_s}\sum_{k=1}^{5} A^s_k T^{k-1} \tag{11}$$

Therefore we can obtain $C^s_{v,v}$ as follows:

$$C^s_{v,v}(T_v) = \begin{cases} \dfrac{\bar{R}}{M_s}\left(\sum_{k=1}^{5} A^s_k T_v^{k-1} - \dfrac{7}{2}\right), & \text{diatomic} \\ \dfrac{\bar{R}}{M_s}\left(\sum_{k=1}^{5} A^s_k T_v^{k-1} - 4\right), & \text{polyatomic} \end{cases} \tag{12}$$

The species vibrational energy $e_{v,s}$ can be obtained by integrating $C^s_{v,v}$ such that

$$e_{v,s}(T_v) = \int_{T_{ref}}^{T_v} C^s_{v,v}(\tau)d\tau \tag{13}$$

Chemical Kinetics

For accurate modeling of a detonation wave, especially in the detonation front where rapid chemical reactions take place in the shock compressed region, species continuity equations based on the chemical kinetics should be solved together with fluid dynamic equations to account for the possible chemical nonequilibrium. The mass production rate of species s from the chemical reactions can be written as [10]

$$w_s = M_s \sum_{r=1}^{N_r} (\beta_{s,r} - \alpha_{s,r})(R_{f,r} - R_{b,r}) \tag{14}$$

where M_s is the molecular weight of species s, N_r is the number of reactions, $\alpha_{s,r}$ and $\beta_{s,r}$ are the stoichiometric coefficients for reactants and productants, respectively, in the r reaction. $R_{f,r}$ and $R_{b,r}$ are the forward and backward reaction rate of r reaction, respectively, defined by

$$\begin{aligned} R_{f,r} &= 1000\left[K_{f,r}\prod_{s=1}^{N_s}(0.001\rho_s/M_s)^{\alpha_{s,r}}\right] \\ R_{b,r} &= 1000\left[K_{b,r}\prod_{s=1}^{N_s}(0.001\rho_s/M_s)^{\beta_{s,r}}\right] \end{aligned} \tag{15}$$

The factors 1,000 and 0.001 are required to convert from CGS units to MKS units, since most reaction rate data in the literature are found in CGS units.

The forward reaction rate coefficient can be expressed by

$$K_{f,r} = A_{f,r}T^{N_{f,r}}Exp(-E_{f,r}/\bar{R}T) \tag{16}$$

where $E_{f,r}$ is the activation energy of the r-th forward reaction. The values of parameters $A_{f,r}$, $N_{f,r}$, $E_{f,r}$ are usually found in table format according to the reactions involved. The backward reaction rate coefficient is evaluated using the equilibrium constant for the reaction such that

$$K_{b,r} = \frac{K_{f,r}}{K_{c,r}} \tag{17}$$

Vibrational Energy Relaxation

The energy exchange between vibrational and translational modes due to intermolecular collisions has been well described by the Landau−Teller formulation where it is assumed that the vibrational level of a molecule can change by only one quantum level at a time [11, 12]. The resulting energy exchange rate is given by

$$Q_{v,s} = \rho_s \frac{e^*_{v,s}(T) - e_{v,s}}{< \tau_s >} \tag{18}$$

where $e^*_{v,s}(T)$ is the vibrational energy per unit mass of species s evaluated at the local translational−rotational temperature, and $< \tau_s >$ is the averaged Landau −Teller relaxation time of species s given by [10]

$$< \tau_s >= \frac{\sum_{j=1}^{N_s} n_j \tau_{sj}}{\sum_{j=1}^{N_s} n_j} \tag{19}$$

where τ_{sj} is the vibrational−translational relaxation time of species s caused by intermolecular collision with species j, and n_j is number density of species j.

The Landau−Teller inter-species relaxation time τ_{sj} can be obtained in seconds using semi-empirical expression developed by Millikan and White [13] such that

$$\tau_{sj} = \frac{1}{p}Exp\left[A_{sj}\left(T^{-1/3} - 0.015\mu_{sj}^{1/4}\right) - 18.42\right] \tag{20}$$

where

$$\begin{bmatrix} p & ; & \text{pressure in atm} \\ A_{sj} & = & 1.16\times 10^{-3}\mu_{sj}\theta_{sj} \\ \mu_{sj} & = & M_sM_j/(M_s+M_j); \text{reduced mass} \\ \theta_{sj} & ; & \text{Characteristic vibrational temperature of harmonic oscillator} \end{bmatrix}$$

The vibrational energy relaxation rate can be simplified using the following approximation [10]:

$$\sum_s \rho_s \frac{e^*_{v,s} - e_{v,s}}{< \tau_s >} \approx \sum_s \rho_s C^s_{v,v}\frac{T - T_v}{< \tau_s >} \approx \frac{\rho C_{v,v}}{\tau v}(T - T_v) \tag{21}$$

where

$$\frac{1}{\tau_v} = \frac{\sum_s \rho_s/(M_s < \tau_s >)}{\sum_s \rho_s/M_s}$$

This approximation not only reduces the number of species dependent parameters but also simplifies the evaluation of the vibrational relaxation as a single relaxation term multiplied by the difference in the translational and vibrational temperature. When a point implicit formulation is used on the source terms in the numerical algorithm, the above approximation greatly simplifies an implicit treatment of the temperature difference which drives the relaxation process.

Numerical Formulation

Finite-Volume Formulation

A discretized set of equations is derived from the governing partial differential equations using the finite-volume method. The advantage of this method is its use of the integral form of the equations, which ensures conservation, and allows the correct treatment of discontinuities [7]. In the following derivation, the cell-centered approach will be described.

For an arbitrary volume ω, enclosed by a boundary σ, the governing equations in integral form can be written as

$$\frac{\partial}{\partial t}\iiint U\, d\Omega + \oint_\sigma \vec{H}\cdot\vec{n}\, d\sigma = \iiint S\, d\Omega \qquad (22)$$

where

$$\vec{H} = (F, G)$$

The unit vector $\vec{n}$ is normal to the infinitesimal area $d\sigma$ and points outwards. The first step to discretize the above equation is to introduce volume averaged values of the conserved variables and the source term as follows:

$$< U >= \frac{1}{\Omega}\iiint U\, d\Omega, \quad < S >= \frac{1}{\Omega}\iiint S\, d\Omega \quad (23)$$

These volume averaged variables are substituted into the integral form of the governing equations to yield

$$\frac{\partial}{\partial t}(< U > \Omega) + \oint_\sigma (F, G)\cdot\vec{n}\, d\sigma =< S > \Omega \qquad (24)$$

For two-dimensional Cartesian coordinate system where the computational cell is defined by two constant lines of both x and y directions, the surface integral can be split into four contributions, one from each bounding surface. When the index of the cell centered variables is (i, j), the above surface integral can be written as

$$\begin{aligned}\oint_\sigma (F, G)\cdot\vec{n}\, d\sigma &= \iint_{\sigma_{i+1/2}} F\, d\sigma + \iint_{\sigma_{i-1/2}} F\, d\sigma \\ &+ \iint_{\sigma_{j+1/2}} G\, d\sigma + \iint_{\sigma_{j-1/2}} G\, d\sigma \end{aligned} \qquad (25)$$

Then, area-averaged values of fluxes can be defined such that

$$\begin{aligned} < F >_{i+1/2} &= \frac{1}{\sigma_{i+1/2}}\iint_{\sigma_{i+1/2}} F\, d\sigma, \\ < G >_{j+1/2} &= \frac{1}{\sigma_{j+1/2}}\iint_{\sigma_{j+1/2}} G\, d\sigma \end{aligned} \qquad (26)$$

where the bounding surface area $\sigma_{i+1/2}$, $\sigma_{j+1/2}$ actually represent cell face lengths in two-dimensional Cartesian coordinate system. After substituting these definitions of averaging into the equation 24 and dropping brackets, the following discrete form of conservation equations written in two-dimensional Cartesian coordinate system can be obtained.

$$\begin{aligned}\frac{\partial U_{i,j}}{\partial t} &= -\left(F_{i+1/2}\frac{\sigma_{i+1/2}}{\Omega_{i,j}} - F_{i-1/2}\frac{\sigma_{i-1/2}}{\Omega_{i,j}}\right) \\ &- \left(G_{j+1/2}\frac{\sigma_{j+1/2}}{\Omega_{i,j}} - G_{j-1/2}\frac{\sigma_{j-1/2}}{\Omega_{i,j}}\right) + S_{i,j}\end{aligned} \qquad (27)$$

Point Implicit Time Integration

Nonequilibrium flows involving finite-rate chemistry and thermal energy relaxation often can be very difficult to solve numerically because of the stiffness. The stiffness in terms of time scale can be defined as the ratio of the largest to the smallest time scale such that

$$\text{Stiffness} = \tau_{\text{largest}}/\,\tau_{\text{smallest}}$$

where τ can be any characteristic time in the flow field. For reactive flow problems, there can be several chemical time scales and relaxation time scales in addition to the fluid dynamic time scale associated with convection. The stiffness parameter can be as high as order 10^6. The point implicit formulation evaluating the source terms at time level $n+1$ has been an effective method used to numerically integrate stiff systems [14]. The point implicit treatment is known to reduce the stiffness of the system by effectively rescaling all the characteristic times in the flow fields into the same order of magnitude.

Equation 27 is rewritten here with source terms evaluated at the time level $n+1$ as follows:

$$\begin{aligned}\frac{\partial U_{i,j}}{\partial t} &= -\left(F^n_{i+1/2}\frac{\sigma_{i+1/2}}{\Omega_{i,j}} - F^n_{i-1/2}\frac{\sigma_{i-1/2}}{\Omega_{i,j}}\right) \\ &- \left(G^n_{j+1/2}\frac{\sigma_{j+1/2}}{\Omega_{i,j}} - G^n_{j-1/2}\frac{\sigma_{j-1/2}}{\Omega_{i,j}}\right) + S^{n+1}_{i,j}\end{aligned} \qquad (28)$$

The source vector is then linearized about the present time level such that

$$S^{n+1} = S^n + \left(\frac{\partial S}{\partial U}\right)^n \Delta U \qquad (29)$$

When simple Euler time integration is used, substituting this linearization into the above equation and rearranging yields

$$\left[\frac{I}{\Delta t} - \left(\frac{\partial S}{\partial U}\right)^n\right]\Delta U = -F^n_{i+1/2}\frac{\sigma_{i+1/2}}{\Omega_{i,j}} + F^n_{i-1/2}\frac{\sigma_{i-1/2}}{\Omega_{i,j}} - G^n_{j+1/2}\frac{\sigma_{j+1/2}}{\Omega_{i,j}} + G^n_{j-1/2}\frac{\sigma_{j-1/2}}{\Omega_{i,j}} + S^n_{i,j} \quad (30)$$

These equations can be evaluated to get ΔU entirely at the current time level at the expense of matrix inversion containing source term Jacobian.

Temporal accuracy can be added using Runge−Kutta integration schemes instead of first-order accurate Euler integration. The two-step explicit Runge−Kutta time integration schemes can be written as follows:

$$\begin{aligned} U^{n+\frac{1}{2}} &= U^n + \gamma_1 \Delta U^n \\ U^{n+1} &= U^{n+\frac{1}{2}} + \gamma_2 \Delta U^{n+\frac{1}{2}} + \zeta_2 \Delta U^n \end{aligned} \quad (31)$$

where $\gamma_1 = 1.0$, $\gamma_2 = 0.5$, and $\zeta_2 = -0.5$, and the three step scheme is given by

$$\begin{aligned} U^{n+\frac{1}{3}} &= U^n + \gamma_1 \Delta U^n \\ U^{n+\frac{2}{3}} &= U^{n+\frac{1}{3}} + \gamma_2 \Delta U^{n+\frac{1}{3}} + \zeta_2 \Delta U^n \\ U^{n+1} &= U^{n+\frac{2}{3}} + \gamma_3 \Delta U^{n+\frac{2}{3}} + \zeta_3 \Delta U^{n+\frac{1}{3}} \end{aligned} \quad (32)$$

where $\gamma_1 = 8/15$, $\gamma_2 = 5/12$, $\gamma_3 = 3/4$, and $\zeta_2 = -17/60$, $\zeta_3 = -5/12$.

Flux-Difference Split Algorithm

The basic feature of the flux-difference split algorithm is to solve a local Riemann problem at the cell interface in order to determine the cell-face flux. An approximate Riemann problem is used with Roe's scheme, and this approach has been used very successfully. Roe's scheme was originally developed for a perfect gas [15]. An extension of this method to a thermo-chemical non-equilibrium gas was made by Grossman and Cinnella [16], and the flux-difference scheme used here is based on their method.

The approximate Rieman solver is implemented by computing the cell face flux as a summation of the contributions from each wave component.

$$\begin{aligned} F_{i+1/2} &= \frac{1}{2}(F_R + F_L) - \frac{1}{2}\sum_{i=1}^{N_s+4}\hat{\alpha}_i\left|\hat{\lambda}_i\right|\hat{E}_i \\ &= \frac{1}{2}(F_R + F_L) - \frac{1}{2}\left([\![F]\!]_A + [\![F]\!]_B + [\![F]\!]_C\right) \end{aligned} \quad (33)$$

where subscript R and L represent right and left state respectively, λ_i are eigenvalues, E_i are eigenvectors, α_i are corresponding wave strengths, and $\hat{}$ indicates Roe averaged quantity. The $[\![F]\!]_A$ term corresponding to the repeated eigenvalues $\lambda_i = u$ can be written as

$$[\![F]\!]_A = \left([\![\rho]\!] - \frac{[\![p]\!]}{\hat{a}^2}\right)|\hat{u}|\begin{bmatrix}\hat{\rho}_i\\ \hat{u}\\ \hat{v}\\ \hat{e}_v\\ \hat{H} - \hat{a}^2/(\hat{\gamma}-1)\end{bmatrix} + \hat{\rho}\,|\hat{u}|\begin{bmatrix}[\![\rho_i/\rho]\!]\\ 0\\ [\![v]\!]\\ [\![e_v]\!]\\ \theta\end{bmatrix} \quad (34)$$

where

$$\begin{aligned} [\![(\cdot)]\!] &= (\cdot)_R - (\cdot)_L \\ \theta &= [\![e_v]\!] - \sum_{i=1}^{N_s}\hat{\Psi}_i[\![\rho_i/\rho]\!] + \hat{v}[\![v]\!] \\ \Psi_i &\equiv \frac{1}{\tilde{\gamma}-1}\frac{\partial p}{\partial \rho_i} = \frac{R_i T}{\tilde{\gamma}-1} - e_{eq,i} + \frac{u^2+v^2}{2} \\ \tilde{\gamma} &= \frac{\tilde{C}_p}{\tilde{C}_v} = \frac{C_{p,t}+C_{p,r}}{C_{v,t}+C_{v,r}} \\ R &= \bar{R}/M_s \end{aligned}$$

The $[\![F]\!]_B$ and $[\![F]\!]_C$ terms which are contributions from the eigenvalues $\lambda_i = u \pm a$, are found to be

$$[\![F]\!]_{B,C} = \frac{1}{2\,\hat{a}^2}\left([\![p]\!] \pm \hat{\rho}\,\hat{a}[\![u]\!]\right)(\hat{u}\pm\hat{a})\begin{bmatrix}\hat{\rho}_i\\ \hat{u}\pm\hat{a}\\ \hat{v}\\ \hat{e}_v\\ \hat{H}\pm\hat{u}\hat{a}\end{bmatrix} \quad (35)$$

For added spatial accuracy, higher-order approximation using the MUSCL approach can be applied. When the MUSCL approach is employed, the primitive variables of right and left states at the cell interface are evaluated using the following extrapolation formulas [7]:

$$\begin{aligned} q^L_{i+1/2} &= q_i + \frac{1-\kappa}{4}\bar{\delta}^+ q_{j-1/2} + \frac{1+\kappa}{4}\bar{\delta}^- q_{j+1/2} \\ q^R_{i+1/2} &= q_{i+1} - \frac{1+\kappa}{4}\bar{\delta}^+ q_{j+1/2} - \frac{1-\kappa}{4}\bar{\delta}^- q_{j+3/2} \end{aligned} \quad (36)$$

where q is any primitive variable, superscript L and R represent left and right extrapolation respectively, and the value of κ determines the type of extrapolation method such that

$$\kappa = \begin{cases} -1 & \text{2nd order upwind scheme} \\ 1/3 & \text{3rd order upwind scheme} \\ 1 & \text{2nd order classic centered scheme} \end{cases} \quad (37)$$

In the above equations, the slopes of the variables are limited to prevent nonphysical oscillations and to preserve the TVD(Total Variation Diminishing) property. The limited slopes can be written using minmod limiter as follows:

$$\begin{aligned} \bar{\delta}^- q_{i+1/2} &= \text{min mod}(\delta\, q_{i+1/2}, \omega\delta\, q_{i-1/2}) \\ \bar{\delta}^+ q_{i+1/2} &= \text{min mod}(\delta\, q_{i+1/2}, \omega\delta\, q_{i+3/2}) \end{aligned} \quad (38)$$

The minmod limiter is a function that selects the smallest number from a set when all have the same sign but is zero if they have different signs such that

$$\text{min mod}(x,y) = \begin{cases} x & \text{if } |x| < |y| \text{ and } xy > 0 \\ y & \text{if } |x| > |y| \text{ and } xy > 0 \\ 0 & \text{if } xy < 0 \end{cases} \quad (39)$$

with the limits on ω given as

$$1 \leq \omega \leq \frac{3-\kappa}{1-\kappa} \tag{40}$$

Temperature Calculation

The conserved variables at each cell center are updated using the equation 30 by a matrix inversion scheme. From these conserved variables, new values of the primitive variables, ρ_s, u, v, e_v, E are easily obtained. However, to close the problem, the temperature and vibrational temperature are determined at each iteration cycle. In order to obtain the temperatures, a Newton−Raphson method is used in the following manner [10, 17]:

$$\begin{aligned} T^{(k+1)} &= T^{(k)} + \frac{\rho e - \sum_s \rho_s e_s \left(T^{(k)}, T_v^{(k)}\right)}{\rho C_{v,tr}} \\ T_v^{(k+1)} &= T_v^{(k)} + \frac{\rho e_v - \sum_s \rho_s e_{v,s} \left(T^{(k)}\right)}{\rho C_{v,v}} \end{aligned} \tag{41}$$

While total internal energy e and vibrational energy e_v are directly obtained from the updated conservative variables, species internal energies e_s and vibrational energies $e_{v,s}$ are calculated from the gas model using the current values of both temperatures. The iteration is carried out until converged values of both temperatures are obtained.

Validation Studies

H_2−Air Reaction Model and Local Ignition Averaging

The two-step reaction model proposed by Rogers and Chinitz [18] is used in this study. This model was developed to represent H_2−Air chemical kinetics with as few reaction steps as possible while still giving reasonably accurate global results. This model consists of the following two steps:

$$\begin{aligned} H_2 + O_2 &\longleftrightarrow 2OH \\ 2OH + H_2 &\longleftrightarrow 2H_2O \end{aligned} \tag{42}$$

where the forward reaction rate constants are given by

$$K_{f,r} = A_{f,r}(\phi)\, T^{N_{f,r}} Exp(-E_{f,r}/\bar{R}T) \tag{43}$$

and the pre-exponential $A_{f,r}(\phi)$ is a function of the equivalence ratio ϕ, the fuel-to-air ratio divided by the stoichiometric fuel-to-air ratio. Values of the parameters used in this model are

$$\left[\begin{array}{rcl} A_{f,1}(\phi) &=& [8.917\phi + (31.433/\phi) - 28.950]\, 10^{47} \\ N_{f,1} &=& -10 \\ E_{f,1} &=& 4,865 \quad \text{cal/mole} \end{array}\right. \tag{44}$$

$$\left[\begin{array}{rcl} A_{f,2}(\phi) &=& [2.000 + (1.333/\phi) - 0.833\phi]\, 10^{64} \\ N_{f,2} &=& -13 \\ E_{f,2} &=& 42,500 \quad \text{cal/mole} \end{array}\right. \tag{45}$$

The backward reaction rate can be obtained from

$$K_{b,r} = K_{f,r}/K_{c,r} \tag{46}$$

where the equilibrium constant $K_{c,r}$ is given by

$$K_{c,r} = A_{c,r}\, T^{N_{c,r}} Exp(-E_{c,r}/\bar{R}T) \tag{47}$$

where

$$\left[\begin{array}{rcl} A_{c,1} &=& 26.164 \times 10^3 \quad \text{cm}^3/\text{mole-s} \\ N_{c,1} &=& 0 \\ E_{c,1} &=& 17,867 \quad \text{cal/mole} \end{array}\right. \tag{48}$$

$$\left[\begin{array}{rcl} A_{c,2} &=& 2.682 \times 10^{-3} \quad \text{cm}^6/\text{mole}^2\text{-s} \\ N_{c,2} &=& 1 \\ E_{c,2} &=& -137,930 \quad \text{cal/mole} \end{array}\right. \tag{49}$$

This model is valid for initial temperatures of 1,000−2,000 K and equivalence ratios of 0.2−2.0. Since the chemistry model is not valid below temperature of 1,000 K, an ignition temperature must be specified.

Nitrogen is also counted as a collisional partner in the thermodynamic model and the relaxation process, but not included in the chemical reaction model since the maximum temperature in hydrogen-air reaction does not reach the dissociation temperature of Nitrogen.

Before an actual calculation using the flow solver is made, the chemical kinetic model needs to be examined to see how each species concentration is changing, and on what time scale. This may provide some insight on the stiffness of the system and some clues to establish a flow solver time step that permits species concentrations to follow the correct kinetics.

The mass production rate equation 14 can be independently integrated using the reaction data in equations 43−49 to yield the species mass fraction history. The typical result obtained using a Runge−Kutta integration method is in figure 1. The mass fraction of OH is shown to rise very rapidly as soon as the ignition starts. The OH production reaction is instantaneous at its initial stage and goes to equilibrium very quickly in less than 10^{-11} seconds. After that, the reactions seem to remain in equilibrium until H_2O production reaction begins around 10^{-9} seconds. It is interesting to note that all these major changes in the species concentrations take place within the first 10^{-7} seconds, a time interval that is a typical fluid dynamic time step. Moreover, the integration time step should remain at or below 10^{-12} seconds to ensure stable integration using the Runge−Kutta scheme, and to properly follow the chemical kinetics. This shows the stiffness of the chemical reaction model.

From the above observation, it could be deduced that the integration time step for the flow solver should be the order of 10^{-12} seconds or less to properly include the chemical kinetics. Moreover, it should be much less than this order in regions of OH production. However, it is practically impossible to use this small time step in the flow solver. When using 10^{-12} seconds as a flow solver time step, the order of 10^9 integration steps might be needed to solve a typical detonation wave propagation problem which has a time scale of interest of the order of 10^{-3} seconds. This would result in 10^4

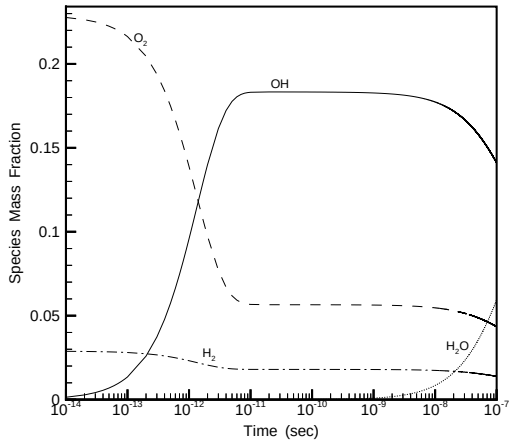

Figure 1: Species mass fraction history from chemical kinetics

days of CPU time when 1 second of CPU time per computation cycle, which is a proper estimate for this code on a typical front-end workstation, is assumed. Fortunately, however, most of this stiffness problem can be taken care of by the point implicit treatment of source terms, through effectively rescaling all the characteristic time scales involved. Thus, a typical fluid dynamic time step of the order of 10^{-7} seconds can be safely used throughout the calculation, since the species production rates during this time interval can be properly treated by the effective rescaling of the chemical reaction time scale.

However, the very first time step where all the drastic changes take place within that short period of time cannot be properly described by rescaling time alone. Another special treatment for the igniting cell is needed to be able to use a typical flow solver time step. For this purpose, a Local Ignition Averaging Model (LIAM) is proposed here. The basic idea of this model comes from the fact that the species mass fractions are changing drastically in a very short period of time as soon as ignition starts, and goes to equilibrium soon afterwards. LIAM seperates the cell in which the ignition condition is met, and then integrates the chemical kinetics equations alone for that cell. A time step less than 10^{-12} seconds is used in the integration within the interval of the flow solver time step. The average production rate of each species during this time interval is then estimated using

$$w_s = \frac{\Delta \rho_s}{\Delta t_f} \tag{50}$$

where $\Delta \rho_s$ is the density change of species s obtained from a separate integration of chemical kinetic equations during this time interval, and Δt_f is the flow solver time step. The average value of the forward reaction rate for each reaction during this time interval can be estimated from the following relations.

$$R_{f,1} = -\frac{W_{O_2}}{M_{O_2}}, \qquad R_{f,2} = \frac{W_{OH}}{2M_{OH}} \tag{51}$$

These terms need to be obtained for the calculation of the source term Jacobian. Here, backward reaction rates during this first reaction time step are assumed to be zero.

LIAM turns out to work well together with the point implicit scheme to accurately describe chemical kinetics in the flow solver using a typical flow solver time step of 10^{-7} seconds. Figure 2 shows calculated results of the species mole fraction history at a fixed location inside the detonation chamber initially filled with hydrogen−air mixture. Excellent agreement can be seen with the equilibrium concentration data from the CEA code [19]. This assures that the chemical kinetics are properly modeled and coupled to the flow solver.

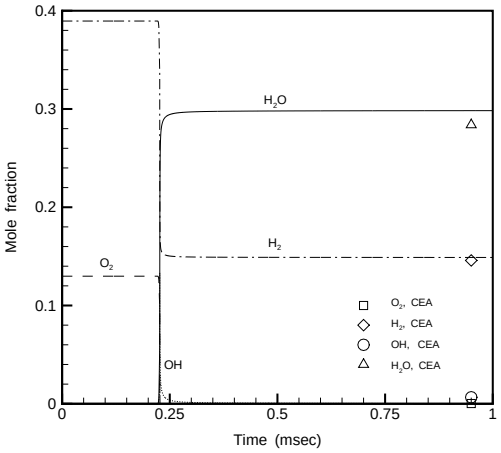

Figure 2: Species mole fraction history from the flow solver

Spatial and Temporal Accuracy

Generally speaking, a higher-order scheme may yield more accurate results, in turn requiring more computing time. The present computer model accommodates the options to choose numerical schemes of both space and time integration up to third-order accuracy. For temporal accuracy, Euler integration for first-order, two-step Runge−Kutta(RK) integration for second-order, and three-step RK for third-order are contained in the model. And for the spatial accuracy, the MUSCL approach is prepared for the higher-order approximations. The purpose of this section is to study the effect of the order of the numerical schemes on the predicted detonation wave. This can then be used to select the order of the scheme necessary to provide adequate resolution of the physical process.

Figure 3 shows a comparison of detonation wave pressure profiles along a detonation chamber when numerical schemes of different order of accuracy are implemented. This figure compares detonation wave profiles, propagating into the quiescent hydrogen−air mixture initially at 1 atmosphere pressure. The higher-order calculation captures the higher peak pressure as expected. However, it is interesting to note that the second-order calculation is close to the third-order cal-

culation, and that the overall shapes of the two waves are almost the same.

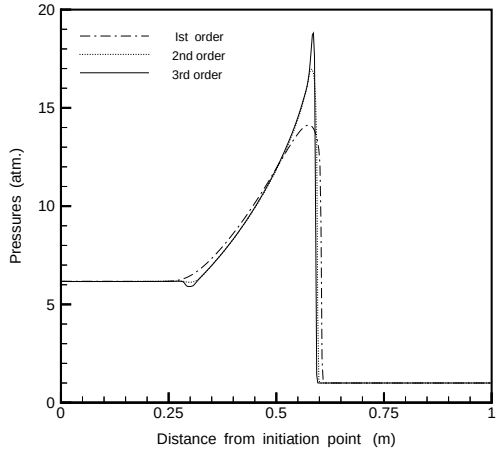

Figure 3: Wave profiles from different order of accuracy

This convergence trend can be seen more clearly in figures 4. This figure shows detonation wave velocities as a function of distance from the initiation point for each scheme. From this observation, a second-order calculation is a reasonable choice when efficiency and accuracy are considered together. Thus, a second-order accurate scheme in both space and time is employed to be used for further calculations, unless otherwise noted.

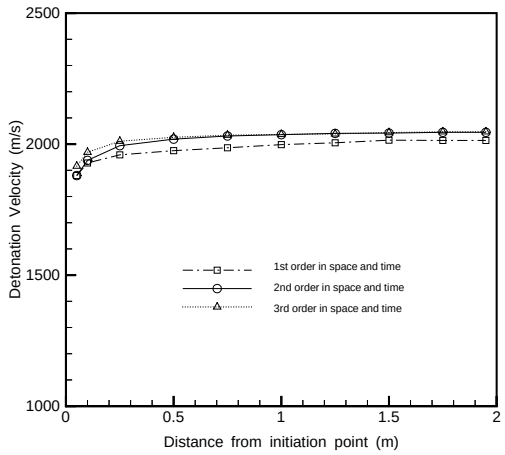

Figure 4: Detonation velocities from different order of accuracy

Mesh Convergence

A mesh convergence test is performed to determine the proper mesh size to insure accurate resolution of the physical process. The same configuration and parameters are used as before but with different mesh sizes. A second-order accurate scheme in both space and time is used throughout the calculation.

Figure 5 shows detonation wave profiles resulting from three different mesh sizes. Actual dimensional sizes of 5.0, 2.5, and 0.5 mm are used, respectively, in modeling a two-meter long tube with planar initiation model. For calculations of both 5.0 and 2.5 mm mesh size, a time step of 10^{-7} seconds has been used successfully to yield stable solutions. However, for the smallest mesh size of 0.5 mm, a smaller time step of 5×10^{-8} seconds has been used, since a time step of 10^{-7} seconds does not yield a stable solution for this mesh size.

The convergence trend can be seen clearly from figure 6 which depict detonation wave velocities along the distance from an initiation point for each mesh size used. The results of 2.5 mm mesh shows almost converged values to the 0.5 mm mesh, in detonation velocity as well as in overall wave shape. If we assume the computing time of 2.5 mm mesh case to be 1 CPU, then the corresponding computing times of 5.0 mm and 0.5 mm case will be about 1/4 CPU and 50 CPU, respectively, for two-dimensional calculation. When we take into account accuracy as well as efficiency in choosing mesh size, mesh size of 2.5 mm can be a reasonable choice.

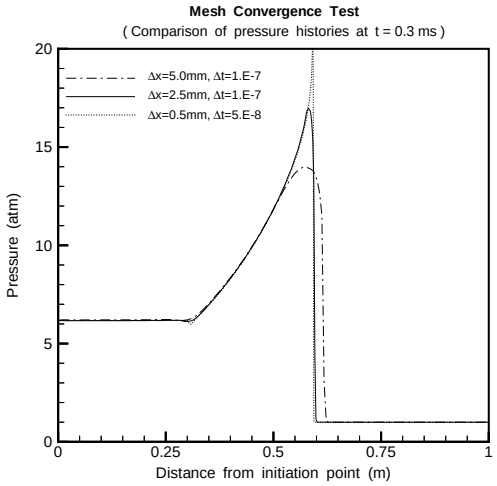

Figure 5: Wave profiles from different mesh sizes

Independence on the Geometry

The properties of fully developed detonation waves should be the same regardless of the geometry involved whenever the initial condition and composition of the fuel−air mixture are the same. Four different calculations are performed here to confirm the results to follow this known postulate. We take four cases with two kinds of geometry and two initiation methods, which are two-dimensional calculations with planar initiation and with point initiation, and repeat for axi-symmetric flow with the same initiation methods. The calculation domain is 68.5 cm × 3.75 cm for both and filled with stoiciometric hydrogen−air mixture. Initiation occurs near the left-end wall.

Figure 7 shows pressure contour plots at specified times for a point initiation case in axi-symmetric geometry. The formation of a planar detonation wave

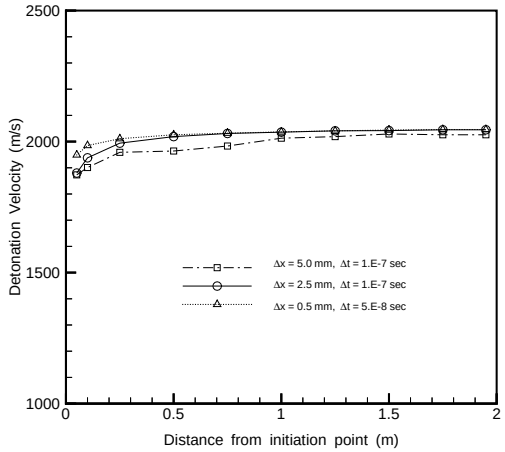

Figure 6: Detonation velocities from different mesh sizes

is clearly captured. A planar wave can be observed to evolve from a spherical wave originated from a point initiation through the interactions of the reflecting waves.

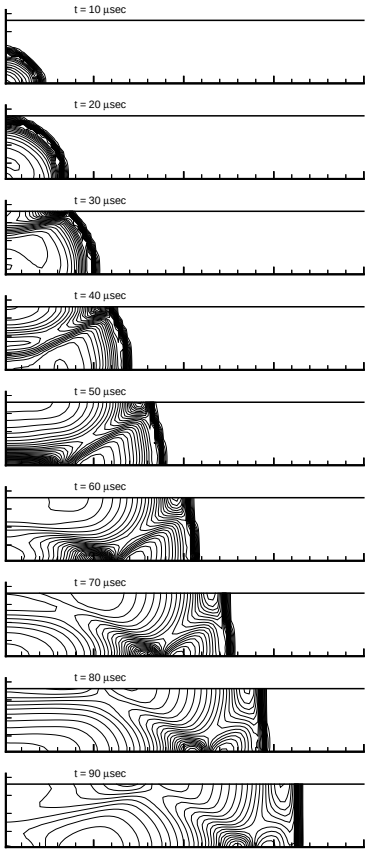

Figure 7: Point initiation in axi-symmetric geometry

The calculated results are summarized in figures 8 and 9. These figures show detonation wave velocities and the CJ plane pressures, respectively, along two different lines which are lower boundary (actually, center line) and upper wall. For point initiation cases, detonation velocities and the pressures on the axis are observed to remain lower than those of planar initiation cases and keep increasing, while the detonation velocities and the pressures on the wall are much higher than those of planar initiation cases and keep decreasing until the formation of the planar wave. The higher pressure and velocity on the wall are due to the reflection of the detonation wave. The detonation velocities and the pressures for all four cases are observed to converge to the same value at a certain distance from the initiation point where fully developed planar waves are formed. And this result confirms the known postulate previously stated.

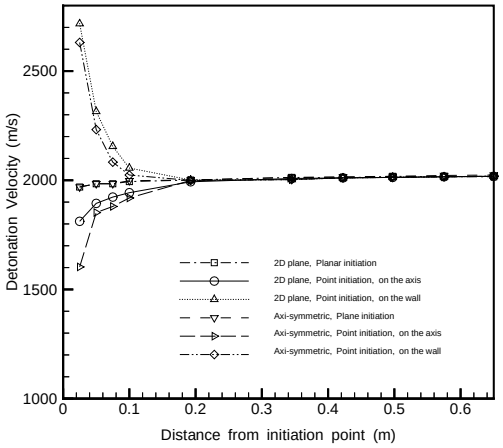

Figure 8: Detonation velocities from different geometries in use

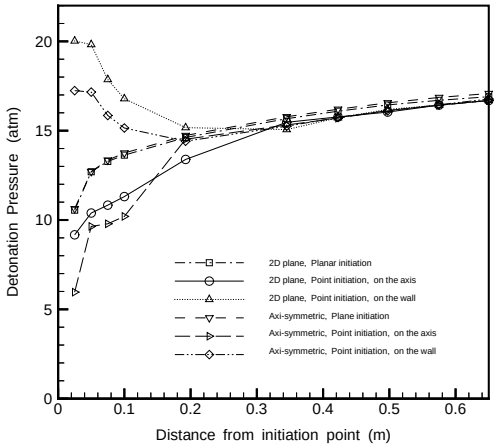

Figure 9: Detonation pressures from different geometries in use

Comparison with Theoretical CJ data

The calculated detonation wave properties are compared with the theoretical CJ data. Since the property

of the fully developed detonation wave is converging to the same value regardless of the geometry involved as seen in the previous section, and since we are interested in the final converged state of the CJ condition, calculations can be properly performed on the one-dimensional planar geometry for the sake of efficiency.

The computational domain is, thus, composed of a detonation tube of semi-infinite length filled with a mixture of hydrogen and air initially at 1 atmosphere and 298.15 K. The detonation is initiated just adjacent to the left-end wall, and the planar wave propagates to the right through the quiescent gas mixture. The detonation wave velocity, pressure, density, and temperature as a function of distance from an initiation point are recorded and compared with the theoretical CJ data. The theoretical CJ data are obtained from the CEA code [19]. The converging trend of all the variables of the detonation wave is confirmed in each calculation of different equivalence ratios. These converged values can be compared to the theoretical CJ data. The results are summarized in figure 10, which depicts the converged values of each detonation variable with varying equivalence ratios, and compares these values with the theoretical CJ data. Excellent agreement between them is observed.

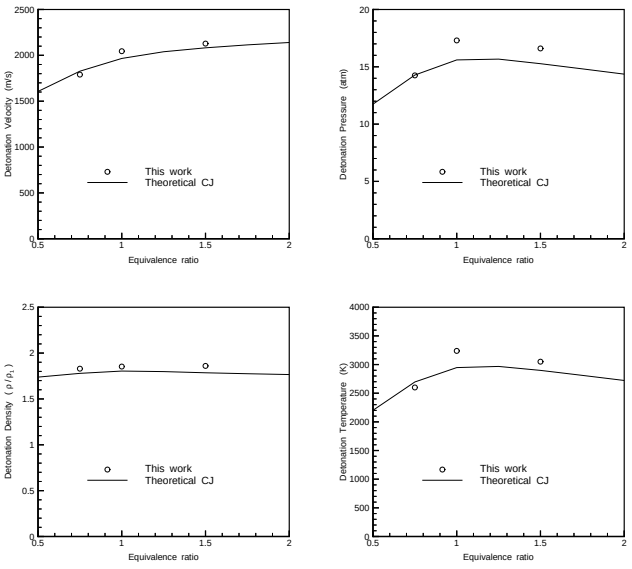

Figure 10: Comparison with theoretical CJ data

Simulation of Shock-Induced Detonation

A series of shock-induced detonation experiments has been performed at The University of Texas at Arlington (UTA). A schematic of the experimental facility is shown in figure 11. The driver tube was highly pressurized with either air or helium, and the detonation tube was filled with a stoichiometric mixture of fuel and oxygen/air. These two tubes were separated by a double-diaphragm section as shown. The pressure histories were recorded at several stations on the wall of the detonation tube during this experiment. The results of a numerical simulation of this experiment are compared with experimental data. This provides validation for the numerical simulation and an aid in understanding the experimental results as well.

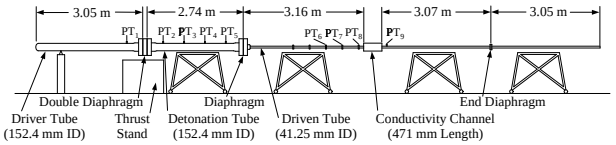

Figure 11: The schematic of the UT Arlington experiment

Figure 12 shows the pressure histories from an experiment, recorded at stations 4 and 5 corresponding to 166.4 cm and 224.8 cm, respectively, from the location of the diaphragm [21]. In this experiment, the initial pressure of the stoichiometric hydrogen-air mixture inside the detonation tube was 3 atm and the driver tube was pressurized initially to 200 atm with helium. Another experimental result from a different shot, but with the exactly same initial set-up is seen in figure 13. These two figures are observed to show almost identical results, and this suggests a reliability of the experimental data. Both the incident detonation wave and the reflected wave were clearly captured at each station. The reflected wave is travelling toward the left after reflecting from the diaphragm separating the driven tube and detonation tube. It is interesting to note that the pressure history after arrival of the reflected wave is observed to increase with additional step-like shapes.

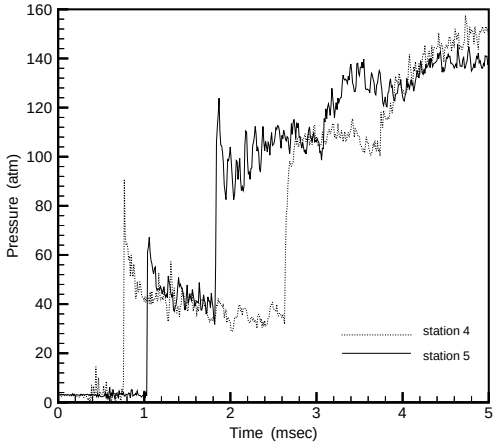

Figure 12: Pressure measurements at station 4 and 5 for test No.14

The modeling of the experiment with a numerical simulation requires that some assumptions and simplifications be made. In this experiment, the double diaphragm section between driver tube and detonation tube measures 11.43 cm long, and is pressurized initially to 100 atm, about a half of the pressure in the driver tube. Therefore, complex wave interactions may exist inside the double diaphragm section and driver

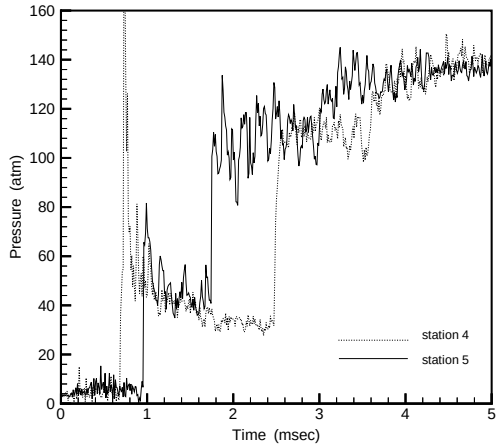

Figure 13: Pressure measurements at station 4 and 5 for test No.23

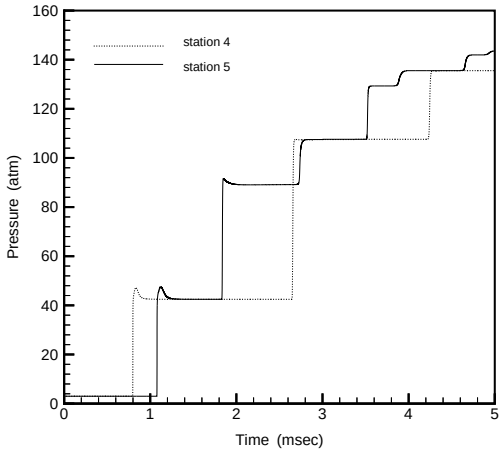

Figure 14: Calculated pressure histories at station 4 and 5

tube until the second diaphragm ruptures and shock-induced detonation is initiated in the detonation tube adjacent to the diaphragm. The details caused by the double diaphragm section are not modeled in the simulation, and instead are replaced by an effective pressure inside the driver tube. This effective pressure is assumed to act directly on the hydrogen-air mixture in the detonation tube as if the diaphragm is effectively removed at $t = 0$. The effective pressure should be lower than the actual initial pressure in the driver tube that was 200 atm in this experiment, and higher than the pressure inside the double diaphragm section that was 100 atm. Therefore, we take 150 atm as a reasonable first guess for the effective pressure in the driver tube.

In the experimental set-up, another diaphragm separated the right-end of the detonation tube and the driven tube. The inner diameter of the driven tube was 4.11 cm, much smaller than the 15.24 cm diameter detonation tube. The right-end of the detonation tube is modeled by a reflective boundary based on the fact that the area opening to the driven tube, even after a rupture of the diaphragm, corresponds to only 7 percent of the cross-sectional area of the detonation tube.

Figure 14 shows the resulting pressure histories at the station 4 and 5 from the simulation using the previously described modeling. It is quite amazing that the simulation result nearly reproduces the experimental data, in spite of the assumptions and simplifications used. The arrival time lag in the incident detonation wave between station 4 and 5 is observed to be almost the same as the experimental measurement, which suggests excellent agreement in the detonation wave velocities. The same agreement is observed in the reflected waves. The pressure levels of both incident and reflected waves are also seen to be in good agreement. It is interesting that the calculated pressure history also shows an increase at each station after the arrival of the reflected wave. The increasing pattern and the level of pressure from the calculation almost exactly reproduce the experimental result.

This step-like increasing pattern of the pressure history is closely examined from the simulation results. Figure 15 shows time evolution of the pressure and the density profiles inside the detonation tube. The incident detonation wave is clearly seen to propagate to the right, and the driver material interface is also clearly observed from the density profile to follow the incident wave. The reflection of the incident wave from the right boundary can be seen in the graph at 1.5 msec, and the reflected wave propagates to the left until it meets the right-running material interface around 2.4 msec. The left-running reflected wave reflects again from the material interface, and as a result, a higher pressure and density are generated from this reflection and propagates back to the right. The material interface travels back toward the left as can be seen in the graphs after 2.4 msec. The right-running wave reflected from the material interface is observed to reflect once again from the right boundary around 3.1 msec and the resulting shock-increased pressure and density are seen to propagate back to the left. From these observations, the step-like increasing pattern of the pressure history turns out to be a result of these multiple wave reflections.

The simulation result using the current numerical model is in excellent agreement with the experimental data. From this observation, the assumptions and the simplifications made to model the experiment are also justified. Especially the effective driver pressure appears to be a reasonable simplification to model the double diaphragm section. This simulation validates the current numerical model to be used with confidence to calculate the unsteady propagation of a detonation wave and its interactions with the boundaries as well as other waves.

Conclusions

A numerical model to simulate the transient combustion process in a pulse detonation engine has been presented. For the purpose of constructing an efficient numerical tool to be used in parametric stud-

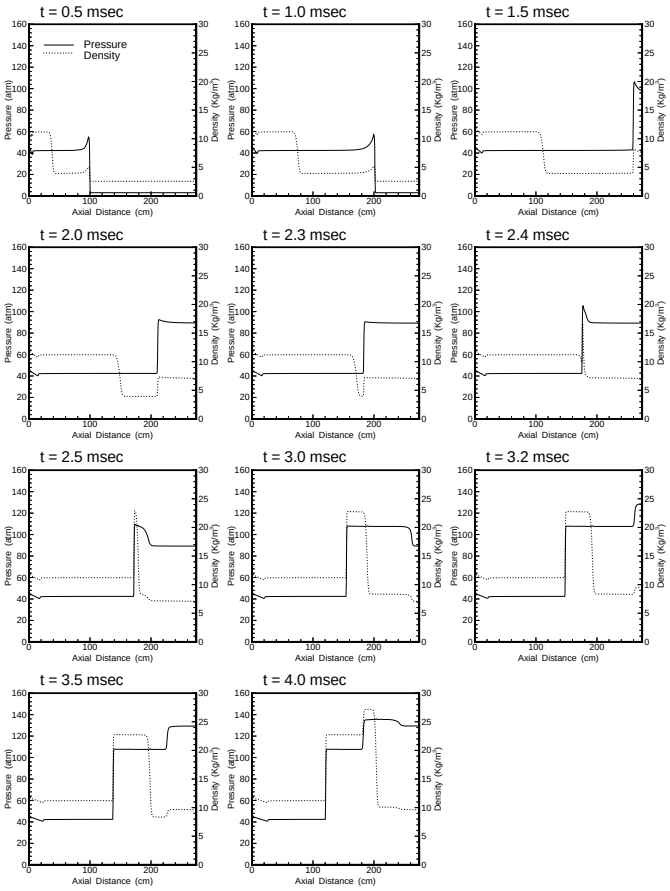

Figure 15: Wave interations in shock-induced detonation tube

ies, while maintaining a reasonable accuracy to be used for analysis, a two-step global model has been selected and validated for the chemcal reactions of a hydrogen−air mixture. The calculated results from the present model have been compared with the theoretical Chapman−Jouguet data and experimental data. Excellent agreement has been observed. These observations validate the efficiency and the accuracy of the present model.

Numerical schemes of different order have been tested both in temporal and spatial accuracy up to the third-order, as well as mesh convergence tests have been performed for different mesh sizes. The second-order accurate scheme in both space and time integration applied to 2.5 mm mesh size seems to be an appropriate choice from the trade-offs of accuracy and efficiency.

Geometry independence of detonation wave properties has been also confirmed as a validation process of the present numerical model.

The shock-induced detonation experiment has been simulated. The calculated result has almost exactly reproduced the experimental data, and this provides a validation of the present model in the unsteady propagation of a detonation wave.

References

[1] Bussing, T. and Pappas, G., "An Introduction to Pulse Detonation Engines," AIAA 94-0263, January 1994.

[2] Bratkovich, T. E. and Bussing, T.R.A., "A Pulse Detonation Engine Performance Model," AIAA 95-3155, July 1995.

[3] Eidelmann, S. and Grossmann, W., "Pulsed Detonation Engine Experimental and Theoretical Review," AIAA 92-3168, July 1992.

[4] Kailasanath K., "Applications of Detonations to propulsion: A Review," AIAA 99-1067, January 1999.

[5] Lynch, E. D. and Edelman R., "Computational Fluid Dynamic Analysis of the Pulse Detonation Concept," AIAA 94-0264, January 1994.

[6] Eidelman, Shmuel, "Pulse Detonation Engine: A status Review and Technology Development Road map," AIAA 97-2740, July 1997.

[7] Tannehill, J. C., Anderson, D. A. and Pletcher, R. H., "Computational Fluid Mechanics and Heat Transfer," 2nd Edition, Taylor and Francis, 1997.

[8] McBride, Bonnie J.; Heimel, Sheldon; Ehlers, Janet G. ; Gordon, Sanford, "Thermodynamic Properties to 6000 K for 210 Substances Involving the First 18 Elements," NASA SP-3001, 1963.

[9] Gordon, Sanford and McBride, Bonnie J., "Computer Program for Calculation of Complex Chemical Equilibrium Compositions, Rocket Performance, Incident and Reflected Shocks, and Chapman−Jouguet Detonations," NASA SP-273, 1971.

[10] Gnoffo, Peter A., Gupta, Roop N. and Shinn, Judy L., "Conservation Equations and Physical Models for Hypersonic Air Flows in Thermal and Chemical Nonequilibrium," NASA TP-2867, 1989.

[11] Candler, Graham V., "The Computaion of Weakly Ionized Hypersonic Flows in Thermo-Chemical Nonequilibrium," Ph.D. Dissertation, June 1988.

[12] Vincenti, W. G. and Kruger, C. H., Jr., "Introduction to Physical Gas Dynamics," Krieger Publishing Company, 1965.

[13] Millikan, R. C. and White, D. R., "Systematics of Vibrational Relaxation," *J. of Chem. Phys.*, No. 39, pp 3209−3213, 1963.

[14] Bussing, Thomas R. A. and Murman, Earll M., "Finite-Volume Method for the Calculation of Compressible Chemically Reacting Floes," *AIAA Journal* Vol. 26, No. 9, September 1988.

[15] Roe, P. L., "Approximate Riemann Solvers, Parameter Vectors, and Difference Schemes," *J. Comput. Phys.* Vol. 43, pp 357−372, 1981.

[16] Grossman, B. and Cinnella P., "Flux-Split Algorithm for Flows with Non-equilibrium Chemistry and Vibrational Relaxation," *J. of Comp. Phys.*, No. 88, pp 131−168, 1990.

[17] Munipalli, R.; Kim, H.; Anderson, D. A.; Wilson D. R., "Computation of Unsteady Nonequilibrium Propulsive Flowfields," AIAA 97-2704, July 1997.

[18] Rogers, R. C. and Chinitz, W., "Using a Global Hydrogen−Air Combustion Model in Turbulent Reacting Flow Calculations," *AIAA Journal* Vol. 21, No. 4, 1983.

[19] Gordon, S. and McBride, B. J., "Computer Program for Calculation of Complex Chemical Equilibrium Compositions and Applications, − I. Analysis," NASA-RP-1311, October 1994.

[20] Lu, F. K.; Kim, C. H.; Wilson, D. R.; Liu, H. C.; Stuessy, W. S. ; Simmons, G. A., "Exploratory Study of Conductivity in Detonation Waves," AIAA 99-0868, 1999

[21] Kim, C. H., Internal test report, Aerodynamics Research Center, The University of Texas at Arlington, 1999.